Phase-Encoded Qualitative Inverse Scattering Approaches to Multistatic Synthetic Aperture Imaging

Matthew J. Burfeindt and Hatim F. Alqadah
US Naval Research Laboratory, Radar Division, USA

matthew.burfeindt@nrl.navy.mil, hatim.alqadah@nrl.navy.mil

ABSTRACT

The phase-encoded linear sampling method (PE-LSM) is an imaging method that avoids the point scatterer model that is common to conventional radar imaging approaches. It thus has the potential for avoiding artifacts when imaging in geometries for which the point scatterer model is less robust, such as scenarios using widely dispersed multistatic sensors. Previous work with the PE-LSM has demonstrated high-fidelity imaging when collecting data with a small multistatic cluster of sensors moving through a synthetic aperture. In this study, we extend this concept to include multiple clusters of sensors in order to obtain the benefits of multiple simultaneous target views. We also explore the use of a monostatic-to-multistatic transformation in this scenario in order to achieve these benefits with as few physical sensors as possible. We apply the PE-LSM to simulated data and compare imaging performance against a conventional backprojection approach. The results demonstrate that applying the PE-LSM to data from multiple sensor clusters can generate images that faithfully represent larger portions of the target. Furthermore, the PE-LSM image results demonstrate significantly greater visual fidelity to the true target surfaces compared to conventional backprojection.

1.0 INTRODUCTION

Conventional imaging strategies based on synthetic aperture radar (SAR) typically use a monostatic data collection. Diversity in the target illumination and observation angles, which is necessary for generating well-resolved two-dimensional imagery, is achieved by translating the single sensor platform across numerous transmit/receive locations. Image fidelity may be inconsistent across sensing scenarios due to physical limitations on the length of the synthetic aperture as well as target-rotation dependence on the received signal.

Multistatic SAR imaging approaches show potential for improving image fidelity by allowing for wider simultaneous diversity of sensing angles and therefore greater diversity of scattering information in the received signal. However, traditional radar signal processing approaches based on backprojection or matched filtering fail to fully exploit multistatic signal content due to their reliance on simplified scattering models in which the scene is assumed to comprise a constellation of discrete, isotropic, point-like scattering centers. Such point scatterer models typically become less robust as the angular diversity of sensor geometry increases (e.g., [1]-[4]). The equivalent scattering center model for a complex target is expected to vary with target view, and thus backprojection processing across a wide variety of transmit or receive angles may result in defocusing or smearing of responses from the target surfaces. In addition, interference effects from the various target surfaces as well as multiple scattering may result in apparent off-body scattering centers that may complicate visual identification of the target shape.

New methods to harness the information content of multistatic data are thus of interest. We have recently introduced a new formulation of the linear sampling method (LSM) for this purpose. The LSM (e.g., [5]-[10]) is a multistatic imaging technique that has received significant attention in the mathematical literature due to its approximation-free scattering model and computational efficiency, but which is difficult to implement in practical scenarios due to its need for a prohibitive number and diversity of multistatic sensor positions. Our formulation, which we denote the phase-encoded LSM (PE-LSM) [11], mitigates this

challenge by disciplining the LSM optimization via propagation-based phase information, thereby allowing for high-fidelity imaging with a more practical sensor distribution. The PE-LSM, like the conventional LSM, implicitly leverages fundamental scattering concepts such as Huygens's principle [6] and equivalent current distributions [7] as opposed to the more simplified point scattering model used by backprojection-based SAR techniques, and therefore has the potential for avoiding common radar imaging artifacts and thereby achieving greater visual fidelity. Both techniques fall under the category of qualitative inverse scattering methods, as they reconstruct only the target shape and not its component electrical properties.

Using both simulated and public experimental datasets, we have demonstrated high-fidelity PE-LSM imaging for scenarios such as the one illustrated in Figure 1(a), in which a single transmitter and a small cluster of receivers collect data while moving in formation across a synthetic aperture [11]. Such scenarios are of interest, as they are potentially practically realizable due to the small number of physical sensors needed while still allowing for more data diversity than a conventional monostatic data acquisition.

In this paper, we expand upon the PE-LSM formulation in order to achieve robust image results with additional flexibility in sensor configuration. First, we explore applying the PE-LSM concept to the scenario illustrated in Figure 1(a) and (b), in which data are collected using multiple independent moving clusters. We generate PE-LSM images for each cluster and fuse the results into a new combined image in order to achieve the benefits of multiple simultaneous views. Critically, we assume that the receivers collect multistatic data only from the transmitter from their own cluster and that the resulting images are fused non-coherently. Thus, we avoid the complication of maintaining coherence across clusters, which supports the potential practicality of the proposed approach.

Second, we further decrease the number of physical sensors by discarding the multistatic receivers in Figure 1 and instead apply the PE-LSM to multiple monostatic sensors. We accomplish this by synthesizing virtual multistatic data via a monostatic-to-multistatic transform (MMT) that was previously introduced in [12]. The MMT makes use of redundancy in multiple-frequency data via an interpolation in the two-dimensional spatial-frequency domain. We apply the PE-LSM technique to the virtual multistatic data in order to evaluate the extent to which we can achieve the benefits of LSM-style imaging using only monostatic data from multiple moving sensors. Using this sensor setup would lower resource cost as well as remove the complexity of maintaining coherence across multiple receivers.

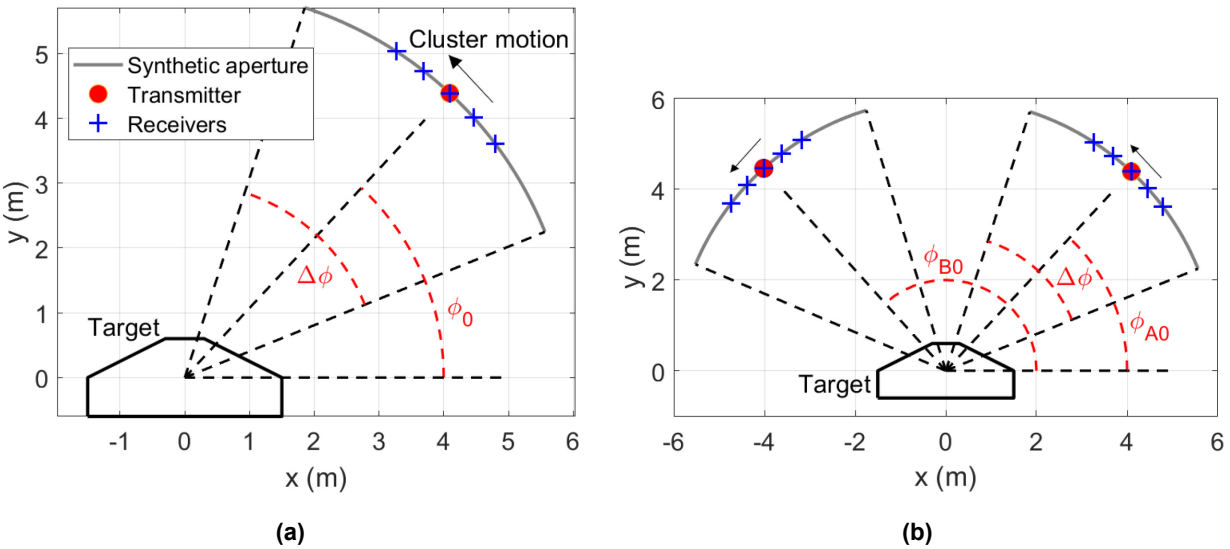

(a) (b)

Figure 1: Diagrams of the multistatic data acquisition scenarios. (a) A single-cluster scenario. (b) A two-cluster scenario. For both scenarios, the angular spacing between adjacent receivers is exaggerated for visualization purposes.

We evaluate the performance of both strategies by applying them to simulated data from a variety of scattering features. We compare the performance of each strategy to each other as well as to conventional backprojection processing. The results demonstrate that using multiple sensor clusters (or multiple monostatic sensors via the monostatic-to-multistatic transform) allows for high-fidelity PE-LSM imaging of larger portions of the target surfaces, thus potentially enabling more robust target identification. The results also demonstrate significant improvements in fidelity of PE-LSM imaging compared to conventional backprojection for images from both multistatic and monostatic data.

2.0 METHOD

2.1 LSM Fundamentals

The LSM operates by solving a linear system of equations for each pixel in the imaging scene and for each frequency of interest. The problem can be posed as finding a complex weighting on the transmitted signal that induces the target to scatter a desired field pattern centered on the interrogated pixel. From an electromagnetic perspective, it can be shown that the target can efficiently scatter the desired pattern only if there is target material in the vicinity of the pixel with which to form equivalent volume or surface currents to re-radiate the corresponding fields [7]. Larger incident-field weightings are thus required for inducing the desired patterns for interrogated pixels that are outside the target volume (and thus remote from potential equivalent currents) as opposed to pixels that are inside the target volume. The solution-norm behaviour can thus be used to identify the target support. The benefits to this imaging approach are that no simplified scattering approximations are required to motivate this treatment and that computation can be achieved in a straightforward manner via linear optimization.

Our mathematical formulation of the LSM is as follows. For ease of explication, we assume two-dimensional, transverse-magnetic propagation. We assume a collection of N_{tx} transmit positions and N_{rec} receive positions distributed around a target of unknown geometry. The multistatic scattered electric field phasors at wavenumber k for each transmit-receive position combination are collected into the $N_{\mathrm{rec}} \times N_{\mathrm{tx}}$ matrix $\mathbf{E}(k)$. The structure of $\mathbf{E}(k)$ for the multistatic synthetic aperture scenarios of interest for this study, for which receive data are collected for only narrow angular offsets from each transmit position, is discussed in detail in [11].

The LSM solution for a pixel location $\mathbf{r}$ and wavenumber k, given by the $N_{\mathrm{tx}} \times 1$ vector $\mathbf{g}(k, \mathbf{r})$, is found by solving the following system of linear equations,

$$\mathrm{E}(\boldsymbol{k})\mathrm{g}(\boldsymbol{k}, \mathrm{r}) = \Phi(\boldsymbol{k}, \mathrm{r}), \tag{1}$$

where $\boldsymbol{\Phi}(k, \mathbf{r})$ is the $N_{\mathrm{rec}} \times 1$ vector of Green's functions between $\mathbf{r}$ and each receive location. From (1), it can be seen that solving for $\mathbf{g}(k, \mathbf{r})$ is equivalent to solving for a transmit weighting that transforms $\mathbf{E}(k)$ into the elementary pattern $\boldsymbol{\Phi}(k, \mathbf{r})$.

As noted above, the norm of the LSM solution is expected to be large for $\mathbf{r}$ outside the target and small for $\mathbf{r}$ inside the target [5]. An indicator function of the norm is thus typically used to visualize the target support. Various indicator functions have been used in the literature. In this paper, we use the following indicator,

$$\boldsymbol{I}(\mathrm{r}) = \left(\sum_i \frac{\|\mathrm{g}(\boldsymbol{k_i}, \mathrm{r})\|^2}{\max_{\mathrm{r}'} \|\mathrm{g}(\boldsymbol{k_i}, \mathrm{r}')\|^2} \right)^{-1}, \tag{2}$$

where the sum is over all collected wavenumbers and the norms are over the elements of $\mathbf{g}(k, \mathbf{r})$, i.e., across the transmitters.

2.2 PE-LSM Formulation

The solution-norm behavior described in the previous subsection tends to break down without a prohibitive number and diversity of transmit and receive angles. If either the transmit or receive antennas are distributed sparsely or over a limited aspect, then the LSM image fidelity is expected to degrade. The limited-aspect scenario is particularly challenging for the LSM, as it lacks in its conventional formulation a method for coherent processing across multiple frequencies, which is the primary method for achieving range resolution in radar signal processing. Modification of the conventional algorithm is thus necessary in order to achieve robust imaging results in many practical sensing scenarios.

A full treatment of the PE-LSM is given in [11]. We briefly describe the formulation here for convenience of the reader. The PE-LSM incorporates two enhancements to the conventional LSM formulation. Both enhancements involve encoding propagation-based phase information into the LSM optimization in order to mitigate a more-limited-than-desired degree of sensor spatial diversity. The first enhancement is the incorporation of a receive-beamforming operation into (1) such that

$$\mathrm{w}^{\mathbf{H}}(\boldsymbol{k},\mathrm{r})\mathrm{E}(\boldsymbol{k})\mathrm{g}(\boldsymbol{k},\mathrm{r}) = \mathrm{w}^{\mathbf{H}}(\boldsymbol{k},\mathrm{r})\Phi(\boldsymbol{k},\mathrm{r}), \tag{3}$$

where $\mathbf{w}(k,\mathbf{r}) = \exp\left(-jk\mathbf{d}_{\mathbf{rec}}(\mathbf{r})\right)$ is a beamforming weight for focusing the receive array at $\mathbf{r}$ and $\mathbf{d}_{\mathbf{rec}}(\mathbf{r})$ is the vector of distances between $\mathbf{r}$ and the receive locations. The beamforming operation filters out reflections from features remote from $\mathbf{r}$, thereby reducing the complexity of the inverse problem so that it can be more robustly solved with fewer measurements.

The second enhancement is a constraint on the phase of the solution to (3). The constraint is implemented via the minimization given by

$$\min_{\mathrm{g}(\boldsymbol{k},\mathrm{r})} \sum_{i} \left|\mathrm{w}^{\mathbf{H}}(\boldsymbol{k}_i,\mathrm{r})\left(\mathrm{E}(\boldsymbol{k}_i)\mathrm{g}(\boldsymbol{k}_i,\mathrm{r}) - \Phi(\boldsymbol{k}_i,\mathrm{r})\right)\right|^2 + \boldsymbol{\alpha}\|\mathrm{g}(\boldsymbol{k}_i,\mathrm{r})\|^2 + \boldsymbol{\beta}\|\gamma(\boldsymbol{k}_i,\mathrm{r})\|^2. \tag{4}$$

In (4), the residual to (3) is minimized subject to two constraints. The first, weighted by regularization parameter α, is a penalty on large-norm solutions that is also included in conventional Tikhonov regularization schemes. The second, weighted by regularization parameter β, is the constraint on the phase defined as

$$\gamma(\boldsymbol{k},\mathrm{r}) = \mathrm{g}(\boldsymbol{k},\mathrm{r}) - \mathrm{g}(\boldsymbol{k}+\boldsymbol{\Delta k},\mathrm{r}) \odot \exp\left(-j\boldsymbol{\Delta k}\mathrm{d}_{\mathbf{tx}}(\mathrm{r})\right), \tag{5}$$

where Δk is the spacing between adjacent wavenumbers, '$\odot$' represents elementwise multiplication, and $\mathbf{d}_{\mathbf{tx}}(\mathbf{r})$ is the vector of distances between the transmit locations and $\mathbf{b}$. This constraint encourages solutions such that the phase change across frequencies matches the change in electrical distance traveled by the incident wave from the array to the pixel. It incorporates the *a priori* assumption that the incident field weighting required to satisfy (3) is very similar across two closely spaced frequencies except for a propagation phase that can be compensated in a straightforward manner. By linking the solution phase across frequency, we effectively incorporate coherent processing into the LSM formulation, thereby allowing for improved range discrimination.

2.3 Monostatic-to-Multistatic Transform

The multistatic data as collected in $\mathbf{E}(k)$ is given in terms of wavenumber and sensor spatial location (the latter defined according to the mapping from receive and transmit location to the matrix row and column, respectively). The data may alternatively be represented in the two-dimensional spatial-frequency domain. In this domain, it is apparent that under the Born (or weak scattering) approximation there is significant redundancy across data samples.

In [12], an MMT strategy was presented to exploit this redundancy to generate virtual multistatic data from monostatic samples. In this paper, we apply the PE-LSM to MMT-generated virtual data for the synthetic

aperture scenario in Figure 1. We present a brief explication of the MMT in the context of the scenario of interest as follows. Further description of the method can be found in [12].

For the scenario pictured in Figure 1(a), let ϕ be the azimuthal angle of the transmitter, measured counter-clockwise from the +x-axis. Let the azimuthal angle of one of the receivers be $\phi + \delta$, such that δ is the constant angular offset between the transmitter and receiver. Let the scattered electric field phasor for transmit angle ϕ, receive angle $\phi + \delta$, and wavenumber k be denoted $E(\delta, \phi, k)$. Each discrete sample of $E(\delta, \phi, k)$ represents an element of matrix $\mathbf{E}(k)$ that is used in the PE-LSM to solve (4), where ϕ determines the element column and $\phi + \delta$ determines the element row.

For convenience, we use the plane-wave approximation and the Born approximation to express the scattered field phasor as

$$E(\delta, \phi, k) \approx \xi \iint \exp(-jk_x x) \exp(-jk_y y) \rho(x, y) dx dy, \tag{6}$$

where $\rho(x, y)$ is the target contrast profile with the background, ξ is a non-informative and slowly varying scale factor, and the x- and y- wavenumbers are given by

$$\begin{aligned} k_x &= -k(\cos\phi + \cos(\phi + \delta)) \\ k_y &= -k(\sin\phi + \sin(\phi + \delta)). \end{aligned} \tag{7}$$

From (6), we can see that there is a two-dimensional Fourier transform relationship relating $\rho(x, y)$ and $E(\delta, \phi, k)$. From (7) we can see that the locations of scattered signal components in two-dimensional Fourier space are determined by the angular locations swept by the sensors as well as by the frequencies of operation.

Figure 2 gives an illustration for the expected support in the two-dimensional spatial-frequency domain of the signals generated by the sensor clusters from Figure 1a. The monostatic (i.e., $\delta = 0$) data support across all collected frequencies is in the form of an angular section of an annulus. The central azimuthal angle of the annulus is determined by the central azimuthal angle of the synthetic aperture, denoted here as ϕ_0. The angular extent of the annulus is determined by the angular extent of the synthetic aperture, denoted here as $\Delta\phi$. The annulus extends in the radial direction from $2k_{\min}$, i.e., twice the lowest wavenumber in the radar bandwidth, to $2k_{\max}$, i.e., twice the highest wavenumber in the bandwidth.

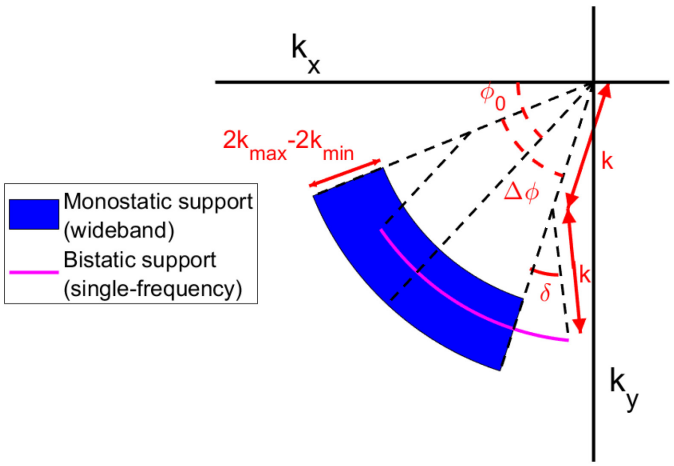

Figure 2: An illustration of the support of the scattered field data in the two-dimensional spatial-frequency domain. In order to highlight the overlap between monostatic and bistatic data, we picture a band of monostatic data and a single-frequency of bistatic data. The bistatic angle offset δ is exaggerated from the value used in this study for visualization purposes.

Also shown in Figure 2 is the bistatic support for a receiver at offset angle δ for a single wavenumber k. The bistatic support traces out a curve with significant overlap with the monostatic data annulus, with some portion of the bistatic data that is outside the monostatic data support due to an angular offset that is a function of δ.

Motivated by this overlap, we generate monostatic data for all ϕ of interest. Then, we synthesize virtual multistatic data for all desired δ and k via interpolating the data in k_x and k_y according to the expected spatial-frequency locations given by (7). (Clearly, not all choices of δ can be synthesized due to the finite extent of the monostatic data). We then populate $\mathbf{E}(k)$ with the collected monostatic and synthesized multistatic samples. All angular samples that cannot be collected or synthesized are left as zeros in $\mathbf{E}(k)$. We then apply the PE-LSM as normal.

Due to the plane-wave and Born approximations in (6) and (7), the synthesis of virtual multistatic data will be imperfect. The effect of approximation- and interpolation-based errors on the PE-LSM image are thus of interest and will be explored in the following section.

3.0 RESULTS

3.1 Simulated Scenario

We generate simulated data for the scenario depicted in Figure 1(b) via the finite-difference time-domain (FDTD) method. We place a highly conducting target near the center of the computational domain. We then define two apertures over which to distribute transmit and receive locations. The radii of the apertures are both 6 m; their central azimuthal angles as measured counter-clockwise from the +x-axis are denoted by ϕ_{A0} and ϕ_{B0} for the lower- and higher-azimuth apertures, respectively; and their angular extents are denoted by $\Delta\phi$.

In each aperture, we uniformly distribute a series of transmit points at 1° increments. We sequentially source each transmit point with a current source and then record the resulting scattered electric fields at a cluster of five receive points centered on the transmit point. The angular spacing between receive points is 2°. We generate frequency-domain phasors from the time-domain scattered electric fields via discrete Fourier transform, resulting in data spanning 1.5 to 1.61 GHz in 5 MHz steps. We apply Gaussian white noise to the phasors such that the total signal-to-noise ratio across all samples is 20 dB. We place the resulting phasors in matrices $\mathbf{E}(k)$ as described in [11]. We generate separate $\mathbf{E}(k)$ for each of the two apertures of data so that the data from each aperture can be processed independently.

3.2 Multistatic Imaging Results

We first apply the PE-LSM and conventional backprojection processing to the collected multistatic data. We apply each technique to the data from each individual aperture. We will refer to imagery from the lower-and higher-azimuth apertures as originating from Clusters A and B, respectively.

For the PE-LSM, we follow a heuristic described in [11] to choose the regularization parameters α and β. We then compute (4) using 6 frequencies uniformly spaced across 1.505 to 1.605 GHz. We generate indicator functions for Clusters A and B, denoted $I_A(\mathbf{r})$ and $I_B(\mathbf{r})$, respectively, using (2). We then form a combined indicator function across the two indicators given by $I_C(\mathbf{r}) = I_A(\mathbf{r}) + I_B(\mathbf{r})$.

For backprojection, we form imagery by computing the following quantity,

$$I^{\mathrm{bp}}(\mathrm{r}) = \left| \sum_i \exp\left(j k_i \mathrm{d}_{\mathrm{rx}}^{\mathrm{T}}(\mathrm{r})\right) \mathrm{E}(k) \exp\left(j k_i \mathrm{d}_{\mathrm{tx}}(\mathrm{r})\right) \right|^2, \tag{8}$$

where $\mathbf{d}_{\mathrm{tx}}(\mathbf{r})$ and $\mathbf{d}_{\mathrm{rx}}(\mathbf{r})$ have the same meaning as in Sec. 2.2. As with the PE-LSM, we form backprojection images for each cluster and then form a combined image via the non-coherent sum given by $I_C^{\mathrm{bp}}(\mathbf{r}) = I_A^{\mathrm{bp}}(\mathbf{r}) + I_B^{\mathrm{bp}}(\mathbf{r})$.

We first present image results for a pyramid target in Figure 3. For this example, $\phi_{\mathrm{A0}} = 47°$, $\phi_{\mathrm{B0}} = 132°$, and $\Delta\phi = 50°$. For the single-cluster images, both the PE-LSM and backprojection images evince high image values along the illuminated edges of the target – i.e., the upper right surface for Cluster A, and the upper left surface for Cluster B. However, the PE-LSM image response is highly concentrated along each surface, whereas the target responses in the backprojection images have significantly worse range resolution.

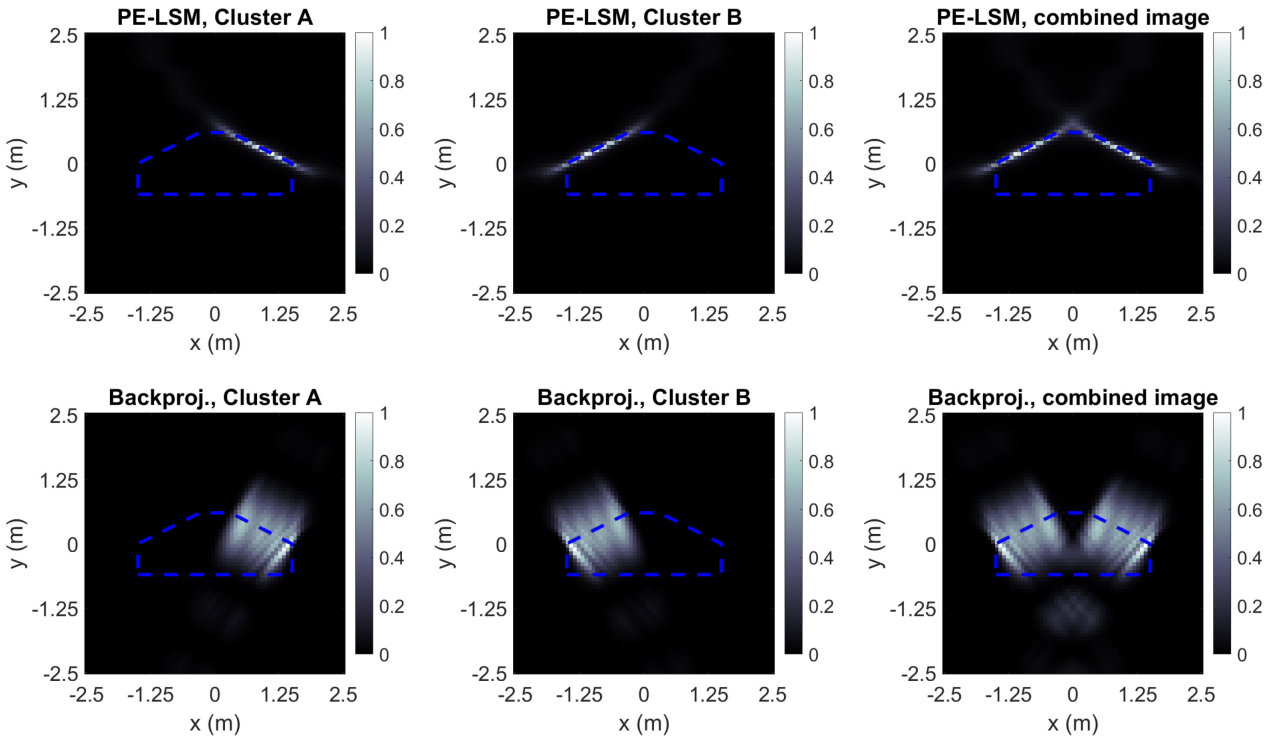

Figure 3: Multistatic PE-LSM images and backprojection images for the pyramid target. The apertures are centered at $\phi_{\mathrm{A0}} = 47°$ and $\phi_{\mathrm{B0}} = 132°$. The colorbar is normalized to the most intense pixel in each image.

In the combined PE-LSM image, both illuminated target surfaces are well-reconstructed at high resolution. This result demonstrates the utility of the proposed multi-cluster approach, as more of the target surface can be reconstructed with high-fidelity by simultaneous illumination from multiple directions. In the combined backprojection image, the two illuminated surfaces are emphasized, again at coarse resolution compared to the PE-LSM results. In addition, there are off-body artifacts below the target caused by the summation of the target responses from both surfaces. These artifacts do not appear in the PE-LSM image, most likely due to its superior apparent range resolution.

Next, in Figure 4, we consider a key-shaped target with two cavities of differing depths. For this example, $\phi_{\mathrm{A0}} = 90°$, $\phi_{\mathrm{B0}} = 175°$, and $\Delta\phi = 50°$. The PE-LSM applied to Cluster A successfully reconstructs the location and size of the bottom surfaces of each cavity, as well as the upper surfaces of the target, albeit at a lower indicator function values. The image from Cluster B faithfully captures the illuminated left edge of the target. The combined PE-LSM image captures all of these features simultaneously, as desired. In contrast, the backprojection Cluster A image is dominated by corner reflector returns within each cavity, while other surfaces appear as interference patterns as opposed to continuous surfaces. The backprojection Cluster B

image evinces the left target edge at lower resolution compared to the PE-LSM image, as in Figure 3. The combined backprojection image is a much poorer visual representation of the illuminated surfaces compared to the combined PE-LSM image.

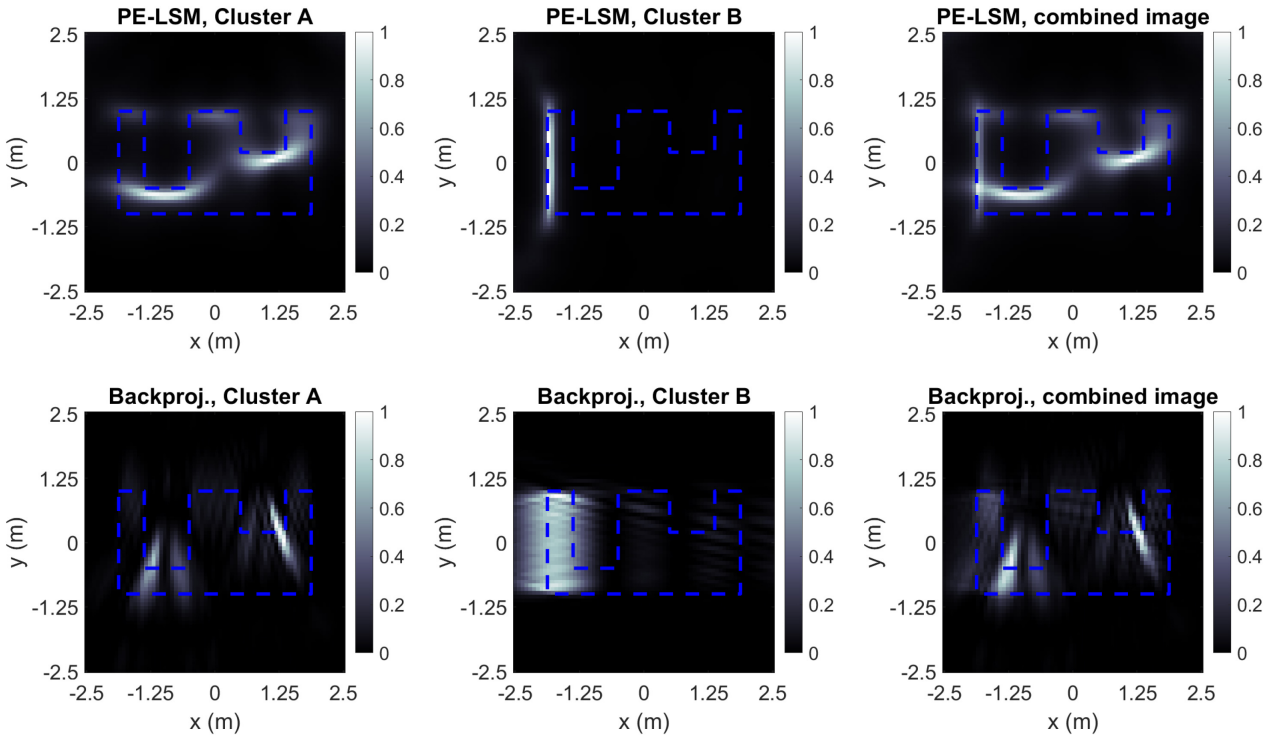

Figure 4: Multistatic PE-LSM images and backprojection images for the key target. The apertures are centered at $\phi_{A0} = 90°$ and $\phi_{B0} = 175°$. The colorbar is normalized to the most intense pixel in each image.

Lastly, we consider a boomerang target in Figure 5. We use $\phi_{A0} = 135°$, $\phi_{B0} = 220°$, and $\Delta\phi = 50°$. As in the previous two examples, the PE-LSM images capture the illuminated target surfaces (i.e., the top and bottom interior arms of the boomerang) with high fidelity and resolution, while the backprojection images capture these surfaces with much coarser resolution. Notably, in the combined backprojection image, a false off-body scattering center appears within the cavity of the boomerang. The false scattering center is caused by interference between the coarse-resolution responses from the two cavity surfaces. In contrast, there is no such effect for the combined PE-LSM image. The avoidance of off-body apparent scattering centers with the PE-LSM is significant, as it may allow for more robust visual identification of the true target shape.

3.3 Monostatic Imaging Results

Next, we consider the performance of the imaging techniques when applied to virtual multistatic data. We discard all collected multistatic samples in all $\mathbf{E}(k)$ matrices, leaving only the monostatic data samples. We then use the procedure described in Sec. 2.3 to generate virtual multistatic samples from the monostatic data. We generate virtual receive channels that match the sensor geometry from Figure 1(b) such that the new $\mathbf{E}(k)$ matrices contain the collected monostatic sample and four virtual receive samples for each synthetic aperture position. We then apply the PE-LSM and backprojection techniques to the data in the same manner as in the previous subsection. We use data from the same three targets and also use identical aperture geometries for each example.

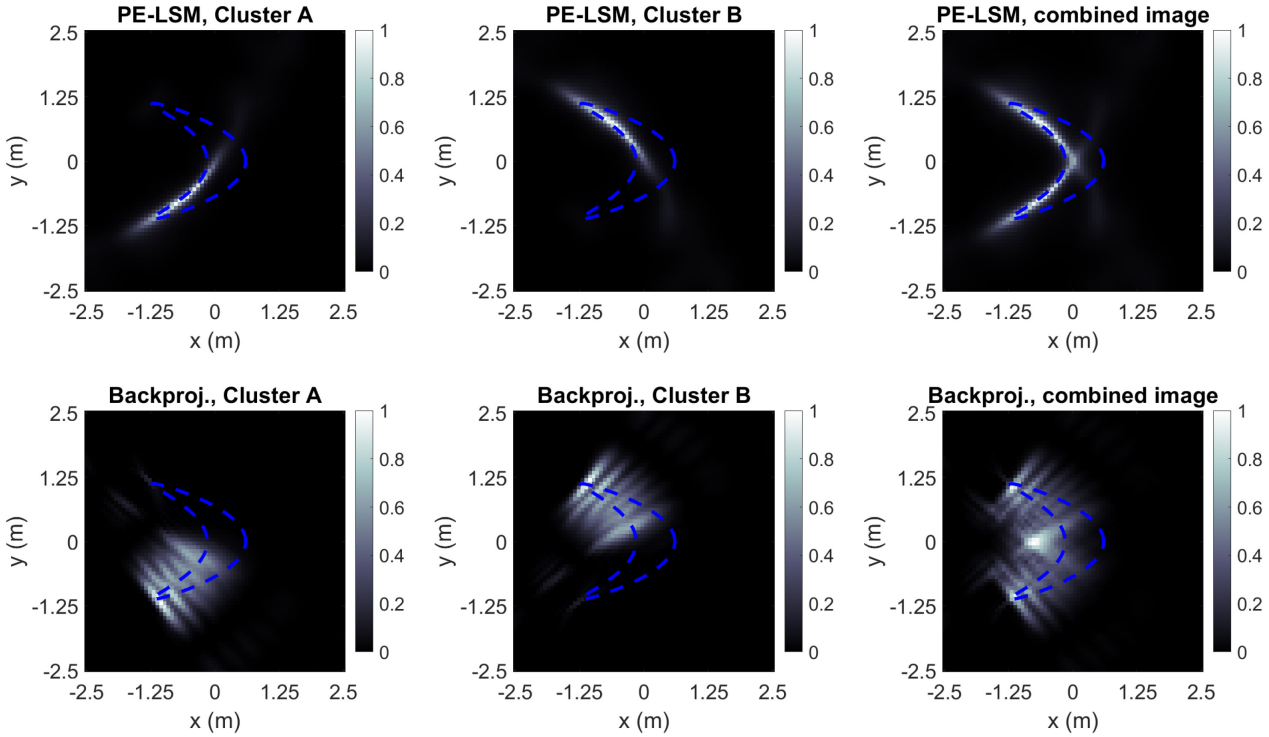

Figure 5: Multistatic PE-LSM images and backprojection images for the boomerang target. The apertures are centered at $\phi_{A0} = 135°$ and $\phi_{B0} = 220°$. The colorbar is normalized to the most intense pixel in each image.

For brevity, we present only the combined image results in Figure 6. The results from virtual multistatic data are very similar to the results from true multistatic data in all cases, with some minor differences. For the PE-LSM image of the pyramid target, the low sidelobe-like tails that extend diagonally from the main target responses are modestly more intense in Figure 6 as compared to Figure 3. For the PE-LSM boomerang image, the intersection of the two main surface responses is deeper inside the target volume in Figure 6 as compared to Figure 5. These effects may be artifacts of the imperfect assumptions in (6) and (7) used for the MMT interpolation. However, these differences are relatively minor, which supports the validity of the MMT approach. These results demonstrate the promise of using multiple monostatic sensors to generate high-fidelity target imagery using the PE-LSM.

4.0 CONCLUSION

In this paper, we extended the phase-encoded linear sampling method (PE-LSM) to synthetic aperture scenarios using multiple small multistatic clusters of sensors. The rationale for this approach is to achieve the benefits of the PE-LSM, namely, an avoidance of the point-scatterer assumptions of conventional radar imaging, while interrogating the target from multiple directions simultaneously. The results from simulated data demonstrate that PE-LSM images from multiple views can be fused together to generate an image that faithfully represents a larger portion of the target surface compared to imagery from a single sensor cluster. Moreover, the PE-LSM results compare very favorably to imagery generated by conventional backprojection in that they avoid off-body artifacts caused by interfering target responses. We showed that these effects can be achieved when using collected multistatic data as well as virtual multistatic data that were generated from only monostatic samples via an interpolation step in the spatial-frequency domain.

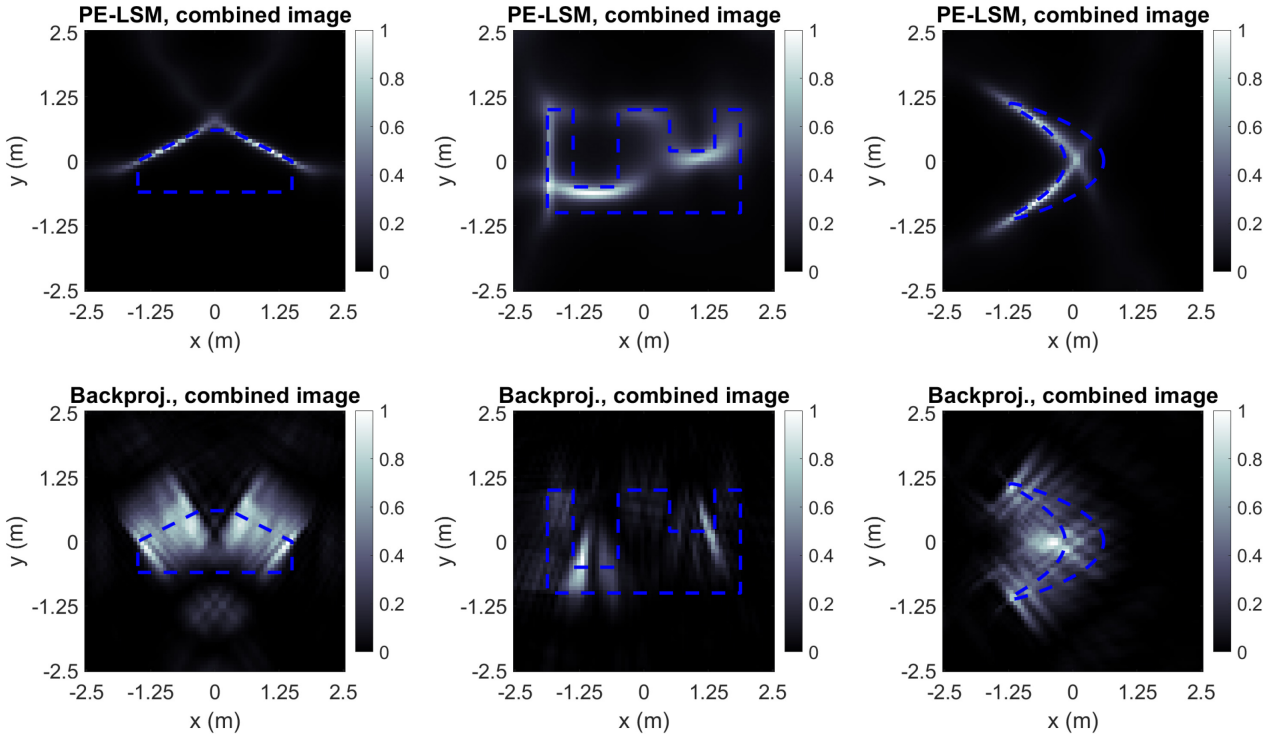

Figure 6: Combined PE-LSM images and backprojection images formed from virtual multistatic data. The colorbar is normalized to the most intense pixel in each image.

The results demonstrate that the benefits of LSM-style imaging may be achieved with very few physical sensors – 10 receivers and two transmitters in the multistatic case and only two monostatic sensors in the virtual multistatic case. Moreover, we demonstrated that we could avoid the complication of making the two sensor clusters coherent by fusing the imagery from each cluster non-coherently. Furthermore, we demonstrated that we could even avoid the complication of making the sensors within a cluster coherent by using only monostatic sensors via the monostatic-to-multistatic transform. The results thus support the practicality and feasibility of high-fidelity PE-LSM imaging from multiple synthetic apertures.

5.0 REFERENCES

[1] J. Ash, E. Ertin, L. Potter, and E. Zelnio, "Wide-Angle Synthetic Aperture Radar Imaging," *IEEE Signal Processing Magazine,* vol. 16, pp. 16-26, 2014.

[2] Y. Zhao, Y. Lin, W. Hong, and L. Yu, "Adaptive imaging of anisotropic target based on circular-SAR," *Electronics Letters*, vol. 52, no. 16, pp. 1406 – 1408, 2016.

[3] R. Hu, R. Min, and Y. Pi, "A Video-SAR Imaging Technique for Aspect-Dependent Scattering in Wide Angle," *IEEE Sensors Journal*, vol. 17, no. 12, pp. 3677 – 3688, 2017.

[4] Randolph L. Moses, Lee C. Pottera, and M. Cetin, "Wide Angle SAR Imaging," in *Proc. SPIE, Algorithms for Synthetic Aperture Radar Imaging XI,* vol. 5247, pp. 164-175, 2004.

[5] F. Cakoni, D. Colton and P. Monk, *The Linear Sampling Method in Inverse Scattering Theory*, Philadelphia, PA: Society for Industry and Applied Mathematics, 2011.

[6] N. Shelton and K. Warnick, "Behavior of the Regularized Sampling Inverse Scattering Method at Internal Resonance Frequencies," *Progress in Electromagnetics Research*, vol. 38, pp. 29-45, 2002.

[7] I. Catapano, L. Crocco and T. Isernia, "On simple methods for shape reconstruction of unknown scatterers," *IEEE Transactions on Antennas and Propagation*, vol. 55, no. 5, p. 1431–1436, 2007.

[8] B. Guzina, F. Cakoni and C. Bellis, "On the multifrequency obstacle reconstruction via the linear sampling method*," Inverse Problems*, vol. 29, p. 125005, 2010.

[9] M. Cheney, "The Linear Sampling Method and the MUSIC Algorithm," *Inverse Problems*, vol. 17, pp. 591-595, 2000.

[10] M. Burfeindt and H. Alqadah, "Boundary-condition-enhanced linear sampling method imaging of conducting targets from sparse receivers," *IEEE Transactions on Antennas and Propagation*, vol. 70, no. 3, pp. 2246-2260, 2022.

[11] M. Burfeindt and H. Alqadah, "Phase-Encoded Linear Sampling Method Imaging of Conducting Surfaces From Full and Limited Synthetic Apertures," *IEEE Open Journal of Antennas and Propagation*, vol. 3, pp. 1191-1205, 2022.

[12] H. Alqadah and M. Burfeindt, "A Far-Field Transformation Procedure for Monostatic Linear Sampling Method Imaging," in *Proc. International Conference on Electromagnetics in Advanced Applications (ICEAA)*, pp. 1387-1392, 2019.